# PROCEEDINGS OF SPIE

SPIEDigitalLibrary.org/conference-proceedings-of-spie

# Iterative reconstruction using Monte Carlo generated system matrix for angle-restricted optical tomography

Torres, Veronica, Li, Chengyue, Brankov, Jovan, Tichauer, Kenneth

Veronica C. Torres, Chengyue Li, Jovan G. Brankov, Kenneth M. Tichauer, "Iterative reconstruction using Monte Carlo generated system matrix for angle-restricted optical tomography," Proc. SPIE 11639, Optical Tomography and Spectroscopy of Tissue XIV, 116391U (5 March 2021); doi: 10.1117/12.2584915



Event: SPIE BiOS, 2021, Online Only

# Iterative reconstruction using Monte Carlo generated system matrix for angle-restricted optical tomography

Veronica C. Torres\*a, Chengyue Lia, Jovan G. Brankovb, Kenneth M. Tichauera
aDepartment of Biomedical Engineering, Illinois Institute of Technology, 3255 S Dearborn St.,
Chicago, IL USA 60616; bDepartment of Electrical and Computer Engineering, Illinois Institute of
Technology, 3255 S Dearborn St., Chicago, IL USA 60616

#### **ABSTRACT**

Filtered backprojection (FBP) reconstruction is a simple and rapid technique for reconstructing tomographic data. Optical projection tomography (OPT) for instance, makes use of this technique to facilitate three dimensional visualization of optically clear biological tissues. However, for the case of nontransparent specimens where scattering dominates, more representative algorithms are required to model the behavior of light through the sample such that the object of interest can be recreated. In this work, model-based iterative techniques are investigated for use with an angle-restricted fluorescence OPT system for the specific application of imaging lymph nodes. Through physical and simulated phantoms, the effects of model inaccuracies in Monte Carlo-generated system matrices was evaluated. Findings demonstrated the importance of accurately capturing detector response, and that sample optical properties were more influential than sample geometry in affecting the reconstructed results.

Keywords: tomographic reconstruction, system matrix, optical projection tomography, angular domain, lymph node

#### 1. INTRODUCTION

Optical projection tomography (OPT) is a favorable modality for imaging biological specimens because three-dimensional visualization is possible using simple filtered backprojection (FBP) reconstruction[1]. This however, requires clear samples such that scattering is essentially eliminated and straight line projections can be assumed. In previous work, we capitalized on the low scattering nature of lymph nodes and the enhanced early photon detection capabilities of angular-domain imaging to facilitate parallel ray projection tomography in whole, nontransparent lymph node assessment[2, 3]. While FBP proved sufficient to detect and localize clinically relevant inclusions, for continued development and improvement of this angular domain early photon tomography (ADEPT) system, more rigorous characterization and image performance assessment was sought. Specifically, we performed a preliminary investigation into the degree of improvement that more complex reconstruction algorithms, namely mesoscopic fluorescence tomography (MFT) approaches[4], could offer. It was determined that model-based iterative reconstruction provided enhancements in image quality[5], so the objective here was to evaluate the sensitivity of the reconstruction results to the assumptions made in generation of the system matrix.

## 2. THEORY

## 2.1 Tomography as a linear problem

The inverse problem of tomographic image reconstruction can be modeled as a system of linear equations given by  $\mathbf{g} = \mathbf{H}\mathbf{f}$ , where  $\mathbf{g}$  is an M-dimensional column vector representing the 2D measured image data;  $\mathbf{f}$  is an N-dimensional column vector of the voxelized object with N of size  $n \times n$ ; and  $\mathbf{H}$  is an  $M \times N$  system matrix that transforms the object data to image data. The measured data,  $\mathbf{g}$ , is made up of m detectors for k different angles, such that M has size  $m \times k$ . Elements of the system matrix,  $h_{ij}$ , each represent the contribution of the voxel j to detector element i. Thus, each row in  $\mathbf{H}$  is the contribution of all voxels to a given detector element, and each column is the vectorized 2D image corresponding to a single voxel. This is represented below:

Optical Tomography and Spectroscopy of Tissue XIV, edited by Sergio Fantini, Paola Taroni, Proc. of SPIE Vol. 11639, 116391U · © 2021 SPIE · CCC code: 1605-7422/21/\$21 · doi: 10.1117/12.2584915

$$\mathbf{g} = \begin{bmatrix} g_1 \\ \vdots \\ g_M \end{bmatrix} \quad \mathbf{H} = \begin{bmatrix} h_{11} & \cdots & h_{1N} \\ \vdots & \ddots & \vdots \\ h_{M1} & \cdots & h_{MN} \end{bmatrix} \quad \mathbf{f} = \begin{bmatrix} f_1 \\ \vdots \\ f_N \end{bmatrix}.$$

#### 2.2 The forward model

The detected fluorescence light field is given by Zhu et al.[6] as a pair of coupled equations:

$$f_{ex}(\mathbf{r}) = \int_{W} G_{ex}(\mathbf{r}_{s}, \mathbf{r}) s(\mathbf{r}_{s}) d\mathbf{r}_{s}, \quad (1)$$

$$f_{em}(\mathbf{r}_{d}) = \int_{W} G_{em}(\mathbf{r}, \mathbf{r}_{d}) x(\mathbf{r}) f_{ex}(\mathbf{r}) d\mathbf{r}, \quad (2)$$

where  $\Omega$  is the object volume, and  $\mathbf{r}$ ,  $\mathbf{r}_s$  and  $\mathbf{r}_d$  are 3D vectors. The first equation of the excitation light field,  $f_{ex}(\mathbf{r})$ , is defined by Green's function  $G_{ex}(\mathbf{r}_s, \mathbf{r})$ , as the propagation of light from a source, s, located at  $\mathbf{r}_s$ , to a location  $\mathbf{r}$ . The second equation,  $f_{em}(\mathbf{r}_d)$ , is the emission light field that describes the propagation of fluorescence light emitted from location  $\mathbf{r}$  and detected by a detector at position  $\mathbf{r}_d$ . This is given by Green's function,  $G_{em}(\mathbf{r}, \mathbf{r}_d)$ , and the fluorescence yield,  $x(\mathbf{r})$ .

#### 3. METHODS

A full description of all methods are detailed in previous work [5], however they will mentioned here in brief.

### 3.1 Monte Carlo simulations and system matrix generation

To model the propagation of light through tissue for generation of a sensitivity matrix, Monte Carlo (MC) simulations were conducted using the open-source MCmatlab program[7]. Simulations were structured to match the design of the ADEPT system. A 780 nm Gaussian LED emitter with a 2.5 cm diameter spot size was used as the source, single detectors were modeled as pencil beams focused at half the volume depth, and average lymph node optical properties ( $\mu_a = 0.3$  cm<sup>-1</sup>,  $\mu_s = 43$  cm<sup>-1</sup>, g = 0.92, n = 1.4) were used throughout a slab volume simulation [Fig. 1(d)]. Pencil beams were representative of the narrow detector aperture used in angle-restricted imaging with the ADEPT system. Analysis using this configuration will be referred to as "closed" aperture. Three-dimensional photon propagation through the sample was modeled and volumetric reconstruction is possible, but 2D analysis was carried out for simplicity.

For 2D reconstruction, a single slice in the middle of the object in the x-y plane, parallel to the optical axis and perpendicular to the axis of rotation was used. Representative source and detector sensitivity profiles are shown in Fig. 1(a) and (b), respectively, where light traveling through the system moves from left to right: from the source, through the medium, and then collection at the detector. The simulated detector profile was translated in one dimension to model a single array of 125 detector elements, and the field of view was reduced to 125 x 125 voxels. Source and detector sensitivity profiles were then multiplied on an element-wise basis to construct individual source-detector pair probabilities [Fig. 1(c)]. Next, each source-detector pair was rotated over 360° in 5° intervals. Elements of each sensitivity profile were vectorized and ordered to generate the total system sensitivity matrix, **H**. For comparison, sensitivity matrices were also generated to model conventional imaging; here, detectors were modeled with isotropically emitting point sources focused at the surface of the sample. Representative detector and resultant source-detector sensitivity profiles are shown in Fig. 1(e) and (f), respectively, and analysis using this setup will be referred to as "open" aperture.

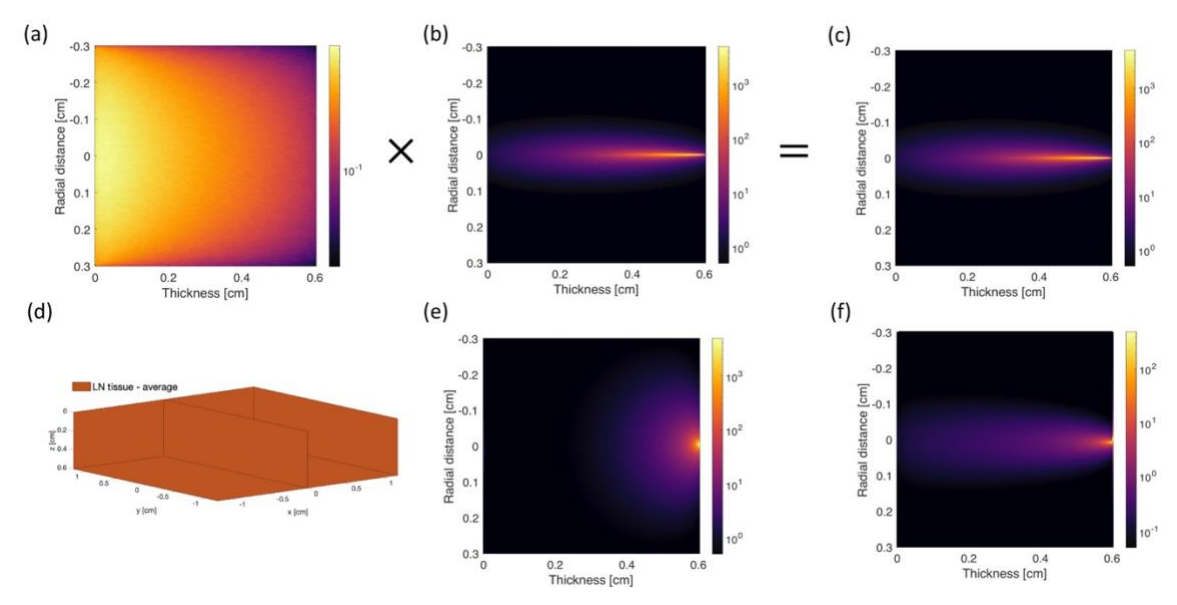


Figure 1. Monte Carlo generated sensitivity profiles presented as normalized fluence rate. (a) Source sensitivity profile. (b) Representative detector sensitivity profile for a closed aperture configuration. (c) Representative angle-restricted imaging source-detector pair sensitivity profile. (d) Sample geometry used in Monte Carlo simulations to produce the sensitivity profiles. (e) Representative detector sensitivity profile for an open aperture configuration. (f) Representative source-detector pair sensitivity profile for conventional imaging with open detector aperture from (e). Light travels from left to right.

#### 3.2 Image reconstruction and test phantoms

Iterative image reconstruction was performed with a non-regularized maximum-likelihood expectation maximization (MLEM) algorithm with a first image estimate of either unity or a FBP reconstruction. These will be designated as MLEM<sub>ones</sub> and MLEM<sub>FBP</sub>, respectively. Reconstruction performance was evaluated with measures of structural similarity (SSIM)[8].

Different MC simulations were run to generate test data for evaluation of reconstruction performance with the proposed system matrix. In addition to the homogenous lymph node mimicking slab shown above, three other geometries with different optical properties were generated – a symmetric block with heterogenous lymph node optical properties [Fig. 2(a), a block structured to mimic the internal structure of a lymph node with heterogenous optical properties [Fig. 2(b)], and a homogenous average lymph node property ellipsoid [Fig. 2(c)]. Simulation volumes are illustrated in Fig. 2, with corresponding optical properties summarized in Table 1.

Two test phantoms were utilized in this work: a physical resin phantom with embedded fluorescence (formation and imaging details found in [9]) and a simulated variable-size inclusion phantom, shown in Fig. 2(d) and (e), respectively.

Table 1. Properties of the media in the tissue volumes used for Monte Carlo simulations at 780 nm. All media are components of lymph node tissue, and assume absorption coefficient  $\mu_a = 0.3 \text{ cm}^{-1}$ , refractive index n = 1.4 and anisotropy factor g = 0.92[10, 11].

Tissue	$\mu_s$ [cm <sup>-1</sup> ]
Average lymph node	43.0
Capsule	46.1
Paracortex	33.34
Medullary sinus	27.02

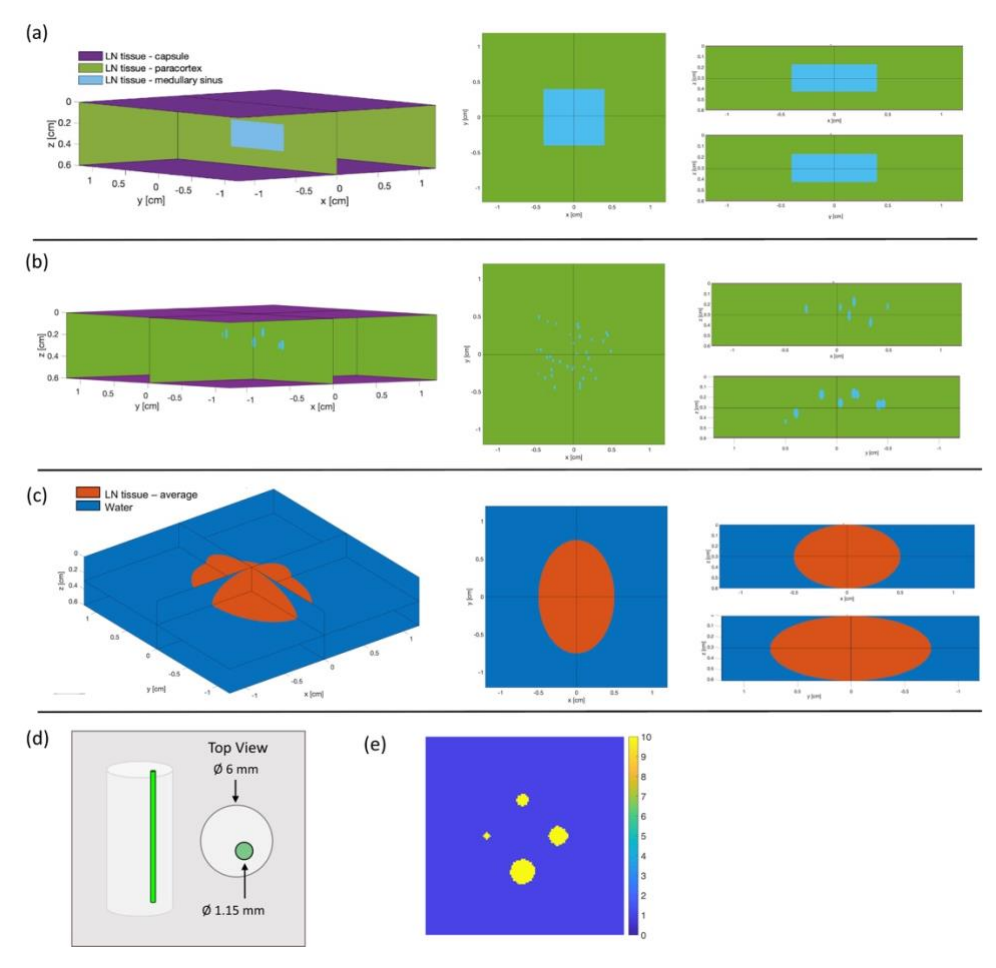


Figure 2. Different configurations of sample geometry used in Monte Carlo simulations to generate system matrices. From left to right, each panel shows the 3D structure, xy-plane, top: xz-plane and bottom: yz-plane. Different colors indicate various tissue types and optical properties. (a) Symmetric block structure with heterogenous optical properties. (b) Heterogenous structure and optical properties. (c) Ellipsoid structure with homogenous optical properties. (d) Illustration of fluorescence-inclusion resin phantom with lymph node-matching optical properties. (e) Variable-size inclusion phantom to test reconstruction algorithms.

# 4. RESULTS AND DISCUSSION

Results indicate that the system-based MLEM reconstructions can offer improved image quality over FBP reconstruction alone. Specifically, with FBP-initialized MLEM, superior contrast and resolution – as indicated with line profile plots across the reconstructed inclusion (results not shown here) – was achieved more rapidly than with ones-initialized MLEM. For the homogenous block-generated system matrix with 72 projections for instance [Fig. 3(a) first two rows), comparable reconstructions were achieved at 50 iterations for MLEM<sub>ones</sub> and 5 iterations for MLEM<sub>FBP</sub>, with the FBP-alone reconstruction shown in Fig. 3(d) for comparison. The advantage of the iterative algorithms was particularly evident when the number of collected projections was reduced to nine. In this case, significant portions of data were missing; consequently, streak artifacts appeared in the FBP reconstruction [Fig. 3(d)]. However, after model-based reconstruction [Fig. 2(a), third and fourth row], the artifacts were increasingly suppressed with greater number of iterations. Again, MLEM<sub>FBP</sub> appeared to achieve this more quickly than MLEM<sub>ones</sub>, but a caveat of the initialization approach was revealed, as initial estimate errors were carried over and amplified. Shown in the 100<sup>th</sup> iteration of the MLEM<sub>FBP</sub> approach, it can be seen that part of the streak artifact near the inclusion was maintained, thereby reducing the reconstructed shape fidelity. In contrast, the MLEM<sub>ones</sub> approach pictured above it was able to preserve the spherical shape.

To evaluate if these results could be improved with a more representative system matrix, the same reconstructions employed above were done using system matrices generated from MC simulations with sample geometry of an ellipsoid rather than a block. These results are shown in the last four rows of Fig. 3(a). Interestingly, the results were very similar to the simple block configuration. From a qualitative assessment, the reconstructions were visibly alike with no obvious image enhancement from either approach, and this was confirmed quantitatively from nearly overlapping line profile plots across the inclusion (results not shown here). This can be expected since optical properties were identical (and low-scattering), and efforts were made experimentally to minimize boundary-interface effects with the use of an indexmatching bath. Moreover, these findings are promising because it suggests that a simple model is sufficient for use in iterative reconstruction and that the system matrix is robust against inaccuracies in sample geometry.

The importance of accurately modeling the detection sensitivity however, is depicted in Fig. 3(b). Here, system matrices were generated to model the ADEPT system and phantom imaging protocol with the exception of the detection sensitivity – an open aperture configuration was modeled instead of a closed aperture (angular domain imaging). Representative detector sensitivity and corresponding source-detector pair profiles are shown in Fig. 1(e) and (f), respectively. Compared to the angular-restricted arrangement shown above it [Fig. 1(b) and (c)], the source-detector pair sensitivity of the open, conventional imaging setup is noticeably more diffuse and an order of magnitude lower. The effect of inaccurately using this model for system matrix generation was manifested as the inability to reconstruct the fluorescent inclusion when using ones-initialized MLEM, and reduced contrast with FBP-initialized MLEM. While MLEM<sub>FBP</sub> had the ability to capture the object, it should be noted that minimal changes were observed even after 100 iterations with 72 projections; and artifact suppression had a strong tradeoff with contrast and resolution for 9 projections.

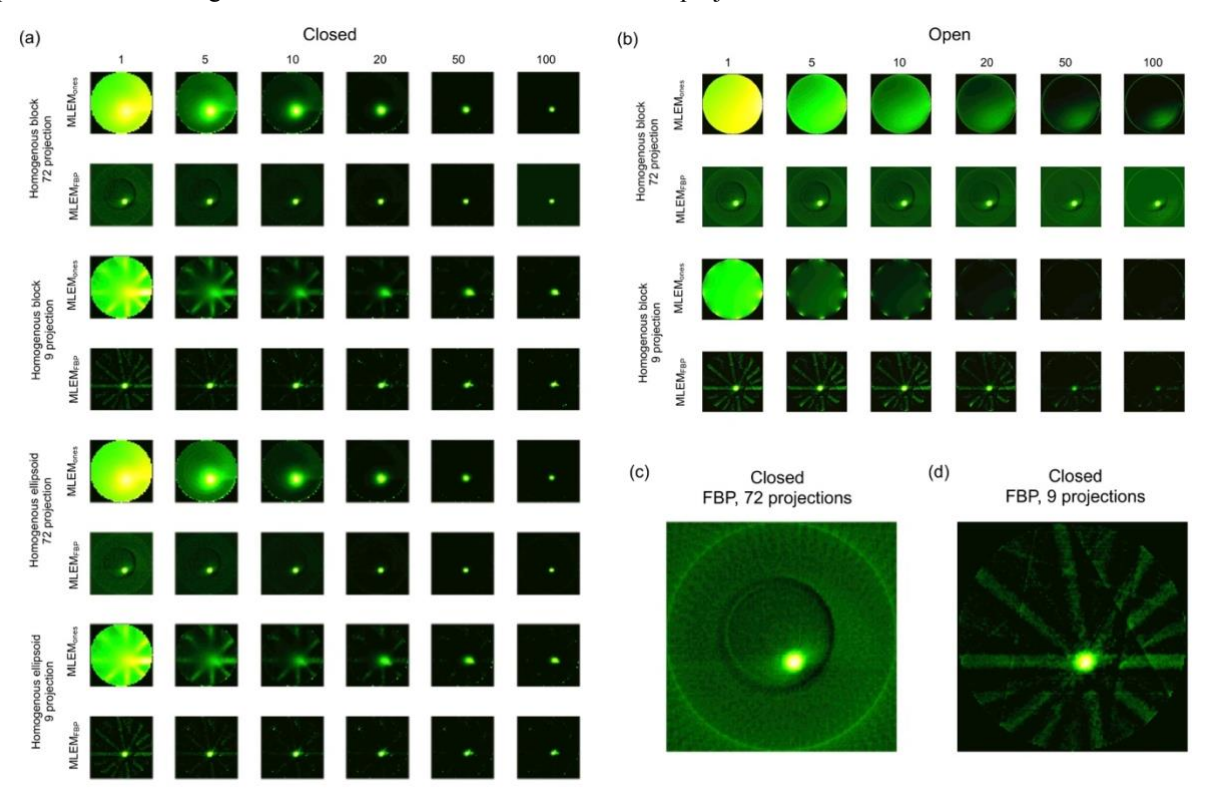


Figure 3. Fluorescence reconstructions generated from ones-initialized (MLEM<sub>ones</sub>) and filtered backprojection-initialized (MLEM<sub>FBP</sub>) maximum-likelihood maximization-expectation algorithms of a fluorescent inclusion embedded in a lymph node matching phantom for different number of iterations, projections and system matrices. (a) System matrices modeled with a closed aperture setup (angle-restricted imaging) consistent with ADEPT imaging used to collect the measured data. (b) System matrices modeled with an open aperture setup (conventional imaging). (c) FBP reconstruction from 72 projection, closed aperture data. (d) FBP reconstruction from 9 projection, closed aperture data. All images were auto-scaled independently for visualization. Columns: iteration number.

To illustrate the impact of this point further, the open and closed system matrices were used for reconstruction of a variable-size inclusion phantom with homogenous optical properties [Fig. 2(e)]. The results are shown in Fig. 4 where the presented reconstruction is the iteration number where the max normalized pixel change in successive image estimates was less than 0.1%. From observation, the open aperture reconstructions clearly suffered from the noise contribution of scattered photons and no inclusions could be resolved. The closed-modeled system on the other hand was able to reconstruct the inclusions, with the FBP-initialized approach outperforming the ones-initialized method that blurred out more of the smallest inclusion.

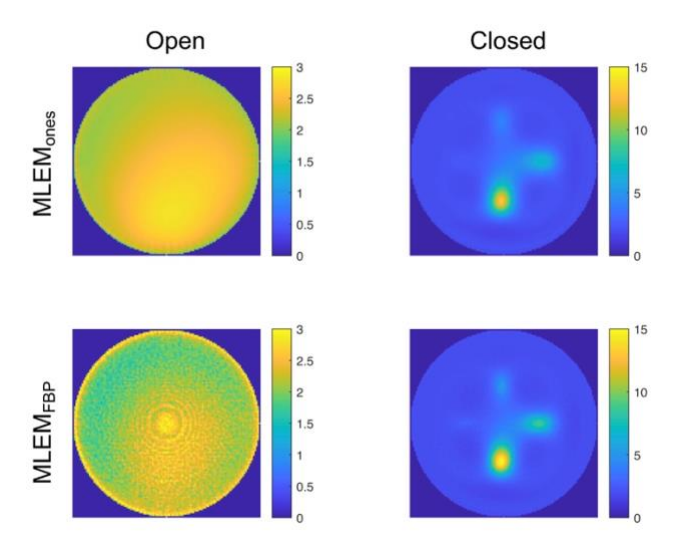


Figure 4. Iterative reconstructions of a simulated phantom [Fig. 2(d)] with homogenous lymph node optical properties for open and closed aperture system setups. First row: ones-initialized MLEM, second row: FBP-initialized MLEM. MLEM: maximum-likelihood expectation-maximization, FBP: filtered backprojection.

The effect of accurate modeling of sample geometry and optical properties was tested for four different systems: (1) homogenous properties and block geometry, (2) heterogenous properties in a symmetric block geometry, (3) heterogenous properties in a random block geometry, and (4) homogenous properties in an ellipsoid geometry. Each was used as the forward model to produce simulated data and reconstructions were done using a system matrix generated from the homogenous block (test system 1). Results are shown qualitatively in Fig. 5(a) and quantitatively in Fig. 5(b) with measures of SSIM. Overall, the findings were visually comparable and consistent with the results presented above with respect to MLEM<sub>ones</sub> and MLEM<sub>FBP</sub> performance. Again, MLEM<sub>FBP</sub> converged toward a solution more rapidly than MLEM<sub>ones</sub>, and the smallest inclusion was better preserved with the former approach compared to the latter. Interestingly, the heterogenous cases appeared to provide better contrast than the homogenous. This can likely be attributed to a lower scattering coefficient ( $\mu_s = 33.3 \text{ cm}^{-1}$ ) in the bulk of the sample as opposed to the average value ( $\mu_s = 43.0 \text{ cm}^{-1}$ ) used in the homogenous case.

Between groups of matching optical properties but different geometry, results were also similar and that was reflected quantitatively in the SSIM plots. That is, the slab with homogenous optical properties and ellipsoid with homogenous optical properties, and the symmetrically distributed heterogenous block and more structurally mimicking heterogenous block with random distribution of medullary sinuses, provided similar results. This suggests that accurate modeling of optical properties is more influential than geometry; but it also reflects the low scattering nature of lymph nodes, such that scattering is minimal and photons travel preferentially straight throughout. The SSIM plot (index of 1 indicates visual perception closer to the true image) showed that MLEM<sub>FBP</sub> outperformed MLEM<sub>ones</sub> for all cases, and that modeling with the homogenous ellipsoid provided the best image quality (mean SSIM MLEM<sub>ones</sub>:  $0.69 \pm 0.02$ , MLEM<sub>FBP</sub>:  $0.72 \pm 0.02$ ). Although the system matrix was not generated for that sample, following the notion of low scattering in lymph nodes, this can be expected because for this geometry, photons simply had less volume to travel through. Reconstructions of the phantom within a homogenous slab had the next best SSIM index (mean SSIM MLEM<sub>ones</sub>:  $0.68 \pm 0.02$ , MLEM<sub>FBP</sub>:  $0.70 \pm 0.02$ ), which was also anticipated because the system matrix was optimized for that model. Next, the heterogenous groups followed with the nonsymmetric geometry outperforming the other (mean SSIM MLEM<sub>ones</sub>:  $0.66 \pm 0.03$ , MLEM<sub>FBP</sub>:  $0.66 \pm 0.03$ , MLEM<sub>FBP</sub>:  $0.69 \pm 0.03$  vs. MLEM<sub>ones</sub>:  $0.64 \pm 0.03$ , MLEM<sub>FBP</sub>:  $0.68 \pm 0.03$ ). Although more heterogenous, this result could

be explained by a more consistent overall bulk owing to the gaps between the medullary sinus regions. Nonetheless, the results presented here demonstrated that the rather simple system matrix used was robust against inaccuracies and sufficient for reconstruction of samples with heterogeneity in optical properties and geometry.

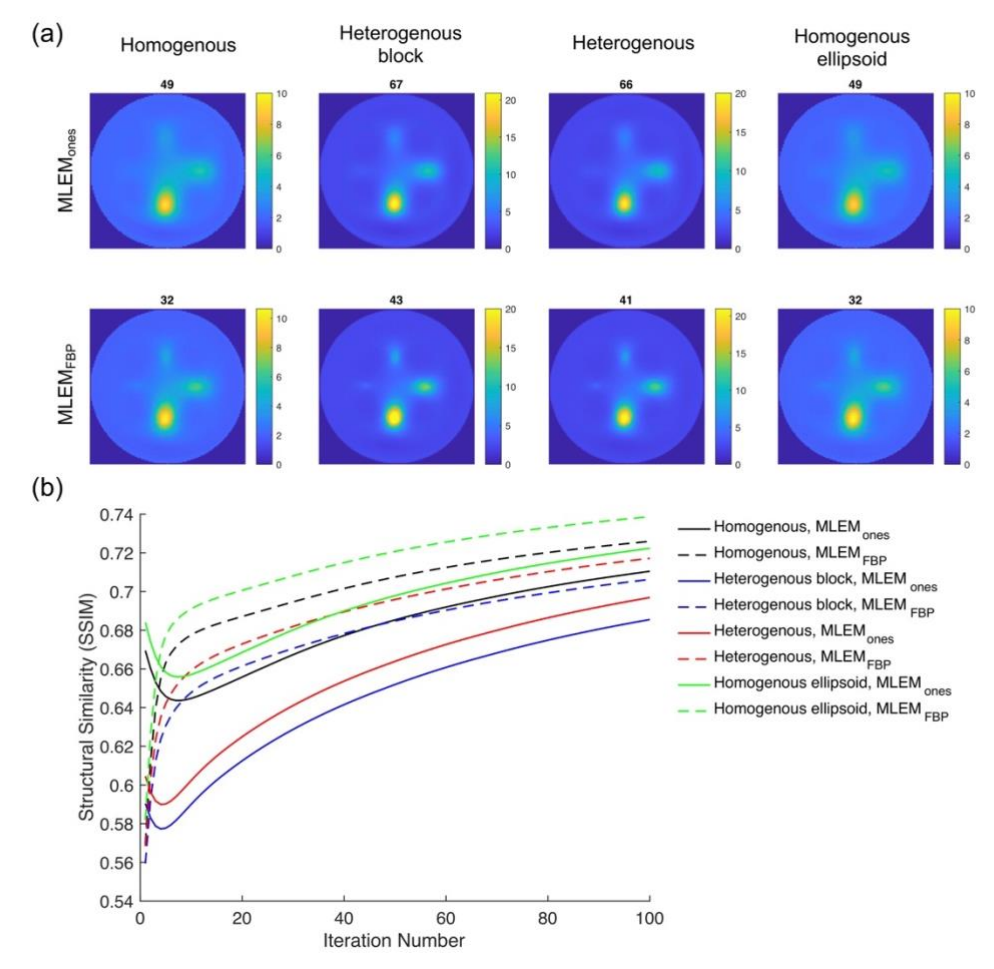


Figure 5. Iterative reconstructions (MLEM<sub>ones</sub> and MLEM<sub>FBP</sub>) of a phantom with different geometries and optical property distributions. (a) Columns from left to right: homogenous properties and geometry [Fig. 1(d)], heterogenous properties and symmetric geometry [Fig. 2(a)], heterogenous properties and geometry [Fig. 2(b)], homogenous properties and ellipsoid geometry [Fig. 2(c)]. Numbers above MLEM reconstructions are the iteration number where the max normalized pixel change in successive image estimates was less than 0.1%. (b) Corresponding plots of structural similarity (SSIM) versus iteration number for different reconstruction methods and phantoms. MLEM: maximum-likelihood expectation-maximization, FBP: filtered backprojection.

#### 5. CONCLUSION

Model based iterative reconstruction using Monte Carlo-generated system matrices is a promising technique for angle-restricted optical tomography. The importance of appropriate system modeling with a narrow aperture for the angular-domain system was exhibited through reconstruction comparison with an "open" aperture setup – inaccurate modeling resulted in unresolvable image reconstructions. It was demonstrated through physical phantom experiments that MLEM algorithms using a FBP reconstruction as the first image estimate were able to improve contrast and resolution, as well as suppress noise and image artifacts compared to FBP reconstruction alone. Moreover, the technique offered the potential for more rapid imaging as image quality improvements were sustained even as the number of collected projections was reduced. Simulated phantoms with heterogeneity were also investigated to test the sensitivity of the system matrix, and it was proven that it was robust against inaccuracies despite being optimized for homogenous properties and simple

geometry. Future work will be required to evaluate the utility of more representative system matrices on biological samples.

#### REFERENCES

- [1] J. Sharpe, "Optical projection tomography," (in eng), *Annu Rev Biomed Eng*, vol. 6, pp. 209-28, 2004, doi: 10.1146/annurev.bioeng.6.040803.140210.
- [2] V. C. Torres *et al.*, "Angular restriction fluorescence optical projection tomography to localize micrometastases in lymph nodes," (in eng), *J Biomed Opt*, vol. 24, no. 11, pp. 1-4, 11 2019, doi: 10.1117/1.JBO.24.11.110501.
- [3] L. Sinha, F. Massanes, V. C. Torres, C. Li, K. M. Tichauer, and J. G. Brankov, "Comparison of time- and angular-domain scatter rejection in mesoscopic optical projection tomography: a simulation study," (in eng), *Biomed Opt Express*, vol. 10, no. 2, pp. 747-760, Feb 2019, doi: 10.1364/BOE.10.000747.
- [4] F. Yang, R. Yao, M. Ozturk, D. Faulkner, Q. Qu, and X. Intes, "Improving mesoscopic fluorescence molecular tomography via preconditioning and regularization," (in eng), *Biomed Opt Express*, vol. 9, no. 6, pp. 2765-2778, Jun 2018, doi: 10.1364/BOE.9.002765.
- [5] V. C. Torres, C. Li, J. G. Brankov, and K. M. Tichauer, "Model-based system matrix for iterative reconstruction in sub-diffuse angular-domain fluorescence optical projection tomography," 2020.
- [6] Y. Zhu, A. K. Jha, D. F. Wong, and A. Rahmim, "Image reconstruction in fluorescence molecular tomography with sparsity-initialized maximum-likelihood expectation maximization," (in eng), *Biomed Opt Express*, vol. 9, no. 7, pp. 3106-3121, Jul 2018, doi: 10.1364/BOE.9.003106.
- [7] D. Marti, R. N. Aasbjerg, P. E. Andersen, and A. K. Hansen, "MCmatlab: an open-source, user-friendly, MATLAB-integrated three-dimensional Monte Carlo light transport solver with heat diffusion and tissue damage," (in eng), *J Biomed Opt*, vol. 23, no. 12, pp. 1-6, 12 2018, doi: 10.1117/1.JBO.23.12.121622.
- [8] Z. Wang, A. C. Bovik, H. R. Sheikh, and E. P. Simoncelli, "Image quality assessment: from error visibility to structural similarity," (in eng), *IEEE Trans Image Process*, vol. 13, no. 4, pp. 600-12, Apr 2004, doi: 10.1109/tip.2003.819861.
- [9] V. C. Torres, C. Li, W. Zhou, J. G. Brankov, and K. M. Tichauer, "Characterization of an angular domain fluorescence optical projection tomography system for mesoscopic lymph node imaging," *Applied Optics*, vol. 60, no. 1, pp. 135-146, 2021/01/01 2021, doi: 10.1364/AO.411577.
- [10] L. Scolaro *et al.*, "Parametric imaging of the local attenuation coefficient in human axillary lymph nodes assessed using optical coherence tomography," (in eng), *Biomed Opt Express*, vol. 3, no. 2, pp. 366-79, Feb 2012, doi: 10.1364/BOE.3.000366.
- [11] V. Torres, T. Wilson, C. Li, L. Sinha, J. Brankov, and K. Tichauer, *Characterization of lymph node optical properties for phantom fabrication* (SPIE BiOS). SPIE, 2019.